THE JOURNAL OF PHYSICAL CHEMISTRY C

Article

pubs.acs.org/JPCC

Electronic Structure of CoO Nanocrystals and a Single Crystal Probed by Resonant X-ray Emission Spectroscopy

Matti M. van Schooneveld,*[,†] Reshmi Kurian,[†] Amélie Juhin,[†,‡] Kejin Zhou,[‡] Justine Schlappa,[‡] Vladimir N. Strocov,[‡] Thorsten Schmitt,[‡] and Frank M. F. de Groot*[,†]

[†]Inorganic Chemistry & Catalysis, Debye Institute for Nanomaterials Science, Utrecht University, Universiteitsweg 99, 3584 CG, The Netherlands

[‡]Paul Scherrer Institut, Swiss Light Source, CH-5232 Villigen PSI, Switzerland

Supporting Information

ABSTRACT: We have performed 2p X-ray absorption (XAS) and 2p3d resonant X-ray emission (RXES) experiments on a CoO bulk single crystal as well as on 4.2 nm CoO nanocrystals. The single crystal data were measured with linearly polarized incident X-rays in the scattering and perpendicular to the scattering plane. An unprecedented total experimental resolution of 100 meV allowed the first X-ray observation of the CoO $^4T_{1g}(^4F)$ manifold that occurs 120 meV above ground state. Detailed theoretical modeling was performed to assess the tetragonal crystal field splitting, spin−orbit, and superexchange parameters for both the single crystal and the nanocrystals. We show that 2p XAS is mainly sensitive to the octahedral field and 3d spin−orbit coupling, while the $^4T_{1g}(^4F)$ manifold in 2p3d RXES probes the tetragonal distortion and the superexchange interactions with high sensitivity. We observe that the nanocrystals have a reduced cubic crystal field splitting and a broadened $^4T_{1g}(^4F)$ RXES manifold that we ascribe to a larger average Co−O distance and an increased magnetic exchange in the nanocrystals. We demonstrate that further improvement of the RXES experimental resolution would not only allow for better disentanglement of the tetragonal distortion, spin−orbit, and superexchange interactions, but it would also allow observing anti-Stokes features in the RXES spectrum.

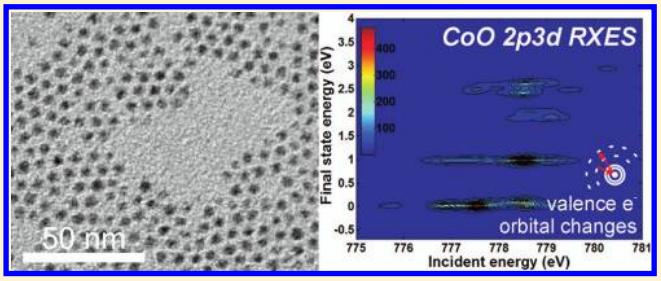

INTRODUCTION

Transition metal oxides are strongly correlated materials with partly filled d bands that lead to unique electronic and magnetic material properties. The colossal magnetoresistance effect in manganese oxides is, for example, widely applied in modern computer data storage,[1] while the cuprates are of interest for their high-temperature superconductivity.[2] In order to understand and control such behavior one ultimately wants to describe the full electronic and magnetic structure of a solid with one unified Hamiltonian H_{solid}. Here we revisit the electronic structure description of cobalt(II) oxide, a prototype material displaying a rich electronic behavior, using 2p3d resonant X-ray emission spectroscopy (RXES) with an unprecedented energy resolution better than 100 meV. Clear differences between CoO nanocrystals and a single crystal were reported.

To elaborate it is necessary to introduce the relationship between a material's electronic structure and (X-ray) spectra. This is given by the Hamiltonian $H_{spectrum} = H_{solid} + H_{radiation} + H_{interaction}$.[3] The radiation field Hamiltonian $H_{radiation}$ describes the quantization of light. It has a negligible influence on the spectra[3] and is neglected in this work. The interaction Hamiltonian $H_{interaction}$ can be related via the Lippmann−Schwinger equation to the transition operator T, the matrix element given in Fermi's Golden Rule.[3] Together with H_{solid} it allows for an adequate interpretation of photon-matter spectra. In XAS and RXES spectra which probe localized final states, H_{solid} can be approximated by the electronic structure definition of a single atom, H_{atom},[3] mainly because the core hole excited state projects the delocalized ground state on a single atom. The full description of H_{atom} depends on many terms, but in XAS and RXES the spectral resolution is to a large extent determined by the lifetime broadening of the electron hole in the final state of the processes,[4] which restricts the level of detail with which H_{atom} needs to be defined. For 2p XAS and 2p3d RXES the final state hole is in the 2p and 3d levels, respectively, and the broadening of the spectra is approximately $\leq$0.4 eV[5] for the first row transition metals in 2p XAS and, based on this work, $\leq$0.1 eV full-width at half-maximum (fwhm) for 2p3d RXES of cobalt(II) in cobalt monoxide. As a consequence, H_{atom} is sufficiently defined by the intra-atomic electron Coulomb exchange interactions, the intra-atomic spin−orbit coupling of the 2p core hole and the 3d electrons, and the interatomic effects described by point charge potentials and caused by neighboring atoms.[6] The relevant potentials are crystal and magnetic superexchange fields accounting for

Received: March 25, 2012
Revised: May 29, 2012
Published: July 2, 2012

electrostatic interactions and the spin−spin coupling. Other interatomic interactions that may need to be considered are metal-to-ligand charge transfer, metal-to-metal charge fluctuations,[7] and lattice phonons or molecular vibrations.

For cobalt(II) monoxide the intra-atomic interactions should be combined with its other material properties. CoO has a cubic NaCl crystal structure in which the Co^{2+} ions have an octahedral symmetry (O_h).[8] It is paramagnetic above its Néel temperature T_N of ca. 290 K.[9,10] Below this temperature the material becomes antiferromagnetic and a tetragonal distortion (D_{4h} symmetry) has been observed.[11] The ground state has an [Ar]$3d^7$ configuration and it is considered to be an insulator of an intermediate type, between a Mott−Hubbard and charge-transfer type.[12] Part of the 3d orbitals are nonbonding or weakly bonding and energetically located in the band gap between the oxygen 2p-orbital-rich valence and the metal 4s,p-orbital-rich conduction band, while the latter also contains antibonding 3d orbitals.[13] This allows for the occurrence of crystal field or d−d transitions as observable by optical absorption spectroscopy in the 1.5−5 eV range.[14] In CoO the crystal field is relatively weak, resulting in a high-spin $3d^7$ configuration, implying that the t_{2g} spin-down orbitals are partly filled and therefore allow for low-energy d−d excitations. Both infrared (IR)[15,16] and 2p X-ray absorption spectroscopy[17,18] have revealed that 3d spin−orbit (ζ_{3d}) coupling is not quenched and have anticipated that this causes the $^4T_{1g}(^4F)$ ground state configuration of CoO in octahedral symmetry to be split in substates over an energy range <150 meV. The tetragonal distortion that occurs below T_N and the superexchange coupling of the antiferromagnetic material induce a further splitting of these energy levels. Furthermore, multiple experiments have shown the existence of (surface) phonons in this energy regime.[16,19,20] Fine structure at energies <150 meV in the infrared spectra[15,16] was interpreted as resulting from 3d spin−orbit coupling, tetragonal distortions, and superexchange interactions, leading to predictions of the strengths of these effects. In contrast to this, 2p X-ray absorption spectroscopy alone cannot determine the strength of these interactions adequately, since often crystal field multiplet calculations using different parameter values can lead to the same 2p XAS spectral shape. Here we will add 2p3d RXES investigations, a useful tool for the electronic structure of metal oxides,[21−24] and present the first X-ray observation of the low-energy manifold derived from the $^4T_{1g}(^4F)$ ground state in CoO. Previously published 2p3d RXES studies of CoO had a spectral resolution of ∼0.5 eV[25] and ∼0.25 eV[26] (against <0.1 eV here) and did not allow for the observation of such fine structure. The results are interpreted with crystal field atomic multiplet calculations. The combined effects of the tetragonal distortion, the 3d spin−orbit coupling, and the superexchange interaction on the calculated 2p XAS and the 2p3d RXES spectra are studied and compared with the benchmark infrared studies. Finally, the present resolution allows for the first observation of differences in the RXES spectra of bulk and nanocrystalline CoO. It is observed that the nanocrystals exhibit a smaller effective crystal field splitting and a broader $^4T_{1g}(^4F)$ RXES manifold as compared to the single crystal, which we ascribe respectively to an increase of the average Co−O distance in the nanocrystals and to an increased average superexchange interaction due to the relatively large surface-to-volume ratio of the nanocrystals.

EXPERIMENTAL SECTION

Materials. *CoO Single Crystal.* The (001) surface exposed cobalt(II) oxide single crystal was prepared by a flame fusion process and obtained from Surface Preparation Laboratory.

ε-Co Nanoparticles. Trioctylphosphine oxide (TOPO; 99%), 1,2-dichlorobenzene (anhydrous, 99%), 2-propanol (anhydrous, 99%), and cyclohexane (anhydrous, 99.5%) were purchased from Sigma-Aldrich. Dicobalt octacarbonyl ($Co_2(CO)_8$; hexane stabilized, 95%), oleic acid (OA; 97%), and acetone (anhydrous, 99.8%) were obtained from Acros Organics. Nitric acid (pro analysis, 65%), hydrochloric acid (fuming, 37%), and hydrogen peroxide (stabilized, for synthesis, 30%) were obtained from Merck. Sulfuric acid (>95%) was obtained from Fischer Chemical. All chemicals were used as received.

CoO Powder. Cobalt(II) oxide (79%) was purchased from Sigma-Aldrich and used as received.

TEM, XRD, and XAS/RXES Tools. Carbon-coated formvar copper grids (200 mesh) for TEM measurements were obtained from Agar Scientific. An airtight XRD specimen holder with dome-like X-ray transparent cap for environmentally sensitive materials (A100B33; sample reception 25 mm diameter, 1 mm depth) was obtained from Bruker AXS. p-Type Boron-doped silicon (100)(111) surface terminated wafers (525 μm thick; cut in 7 × 7 mm^2 squares; resistivity ∼5 Ω cm) were obtained from CrysTec GmbH. Hydrofluoric acid (pro analysis, 48−51%) was obtained from Acros Organics. Plastic tweezers (style KR) were obtained from Rubis Switzerland. Sticky carbon tape was obtained from NEM Nisshin Em.Co.Ltd. Silver epoxy paste (E4110 kit) was obtained from Epoxy Technology.

ε-Co/CoO Nanoparticle Preparation and Size-Selective Precipitation. The CoO nanocrystals are passivated ε-Co/CoO nanoparticles, prepared by exposing ε-Co nanoparticles to air.

ε-Co Nanoparticle Synthesis. For ε-Co nanoparticles, 0.45 g (1.32 mmol) of $Co_2(CO)_8$ was dissolved in 3 mL of anhydrous 1,2-dichlorobezene in an airtight flask. In a separate airtight flask 0.10 g (0.26 mmol) of TOPO and 0.18 g (0.64 mmol) of OA were dissolved in 2 mL of dry 1,2-dichlorobezene. The metal precursor and ligand solutions were prepared under magnetic stirring inside a nitrogen-atmosphere glovebox (H_2O/O_2 levels <2 ppm). In a nitrogen-atmosphere Schlenk line outside the glovebox, a three-necked round-bottomed flask was evacuated and flushed with N_2 gas three times. Subsequently, 10 mL of dry 1,2-dichlorobezene was injected into the flask through a septum and heated until reflux temperature (186 °C; boiling point 1,2-dichlorobezene). Next, the 2 mL of OA- and TOPO-containing solvent and the metal precursor solution were injected, in this order, from airtight vials in the hot 1,2-dichlorobezene. Upon injection the metal precursor solution changed instantaneously from yellow to black. Mixtures were refluxed for 30 min, allowed to cool to room temperature, and transferred back to the glovebox before further analysis.

Note that glassware was cleaned with Piranha etch (3/1 v/v sulfuric acid/hydrogen peroxide), Aqua regia (3/1 v/v nitric/hydrochloric acid), excessive deionized water, and anhydrous acetone prior to synthesis.

Size-selective precipitation of the magnetic ε-Co nanoparticles was done by use of a 1.3 T magnet. For this purpose, typically 1 mL of a raw nanoparticle dispersion was submitted to four size-selective steps with use of increasing amounts of

anhydrous 2-propanol as an antisolvent (0.5, 1, 2, and 4 mL in the first, second, third, and fourth steps). In the first step the solution was put on the magnet to destabilize the largest nanoparticles. The sediment was kept and redissolved in 1 mL of anhydrous cyclohexane for further analysis. To the supernatant the extra amount of 2-propanol was added and the mixture was put on the magnet again. This was repeated until four size-selected batches were obtained in 1 mL of cyclohexane.

ε-Co/CoO Nanoparticles. In order to obtain cobalt monoxide passivated nanoparticles, or ε-Co/CoO core/shell nanoparticles, the metallic ε-Co nanoparticles were exposed to air as described by Wiedwald et al.[27] Time-dependent powder X-ray diffractograms on 10.6 nm ε-Co nanoparticles were used to analyze the oxidation of such particles as shown in Figure S1 in the Supporting Information.

Transmission Electron Microscopy (TEM) and X-ray Powder Diffraction (XRD). Carbon-coated formvar Cu-grids were dipped in nanoparticle dispersions and imaged on a Tecnai 12 (FEI) operating at 120 kV, equipped with a SIS CCD camera Megaview II. ITEM software (Olympus) was used to measure size distributions based on at least 200 particles.

XRD diffraction patterns were acquired on a Bruker D8 advance diffractometer. Cobalt K$\alpha_{1,2}$ X-ray tubes (λ = 1.790 Å) operating at 30 kV were used, with currents of 45 and 10 mA, respectively. Typically, data points were acquired between 40° < 2θ < 110° every 0.2° with 13 s step^{-1}. XRD samples of the metallic ε-Co nanoparticles were prepared inside a glovebox and enclosed in an airtight and X-ray transparent box to probe the nonoxidized, as prepared nanoparticles. After the measurements in the inert atmosphere, the ε-Co nanoparticles were measured without protective cap and exposed to air.

Sample Preparation for X-ray Absorption Spectroscopy (XAS) and Resonant X-ray Emission Spectroscopy (RXES) Measurements. The ε-Co/CoO nanoparticle dispersions were dripped onto silicon wafers for the XAS and RXES measurements. Prior to this the silicon substrates were treated to remove oxygen species from the wafer surface and to passivate the silicon wafers with atomic hydrogen. The wafers were immersed respectively in acetone, 2-propanol, and deionized water and given an ultrasonic treatment for 10 min each. The substrates were then etched, following Thorton and Williams,[28] for 10 min with a 1/5/4 v/v/v solution of HF/ethanol/water. Subsequently, the wafers were rinsed with deionized water to remove physisorbed surfaces species,[29] before drop casting the nanoparticle solutions on the wafers. The wafers were attached with sticky carbon tape to an aluminum holder designed to fit into the experimental synchrotron setup. Silver epoxy paste was applied between the substrate and the transfer tool to improve conductivity. The holder was introduced to the load lock chamber of the ADRESS beamline, which was subsequently pumped down to ~10^{-8} mbar before the sample was transferred to the analysis chamber for XAS and RXES measurements.

XAS and RXES Measurements and Spectral Analysis. Total electron yield (TEY) Co $L_{2,3}$- and O *K*-edge XAS spectra were collected by measuring the drain current of the samples. Total fluorescence yield (TFY) spectra were acquired by using a photodiode close by the samples. The XAS spectra were sampled with 50 points eV^{-1}. The incident energy scale was calibrated measuring the cobalt 2p XAS spectra of the cobalt monoxide powder and comparing it with literature values.[30] The RXES spectra were measured with use of the high-resolution Super Advanced X-ray Emission Spectrometer (SAXES) at the ADRESS beamline of the Swiss Light Source.[31,32] A scattering geometry was used in which the angle between the incoming light vector and the outgoing one was 90°. The incoming light is polarized either linear parallel (depolarized geometry or linear horizontal; LH) or linear perpendicular (polarized geometry or linear vertical; LV) to the scattering plane with a grazing incident angle of 20°. By positioning the beam at a noncobalt-containing and amorphous reference and varying the incoming energy from 765 to 785 eV in steps of 1 eV step^{-1}, the elastic peak was used to calibrate the RXES detector. For this purpose the elastic peaks were fitted with Gaussian functions and the maxima of the fits were plotted against detector-channels. The plot was fitted with a linear curve to determine the energy-channel response function. At the Co L_3-edge (~780 eV) the combined energy resolution of the RXES zero-loss peak was 80 and 96 meV fwhm for the nanocrystal and the single crystal data, respectively. In order to obtain resonant spectra the incident energy was tuned to and over the cobalt L_3-edge. Spectra were sampled with 100 points eV^{-1} and summed over 4−10 partial spectra that were acquired for 10 min each. The pressure in the analysis chamber was lower than 1 × 10^{-8} mbar during all measurements. For the CoO single crystal all measurements were carried out at 10 K and it was aligned with the surface normal (001) in the scattering plane. The measurements on the CoO powder and the CoO nanocrystals were measured at 291 ± 5 K.

Crystal Field Multiplet Calculations for XAS and RXES. Calculations based on the Cowan−Butler−Thole code as developed by Thole et al.[33,34] were used for interpreting the experimental core-hole X-ray spectra. The code enables the origin of the 2p XAS[35,36] and 2p3d RXES transitions to be explained by using atomic multiplets (the 3d−3d and 2p−3d Coulomb interactions, the spin−orbit coupling on every open shell of the absorbing atom), crystal and superexchange fields, and charge transfer processes which can be significant at the transition metal *L*-edge. Note that the interactions occurring at these edges are not well described by modern density functional theory (DFT) methods, while DFT codes would be better suited for the interpretation of other edges (for example, 1s XAS). A freeware interface version of the multiplet code is available under the name Charge Transfer Multiplets for XAS and RXES (CTM4XAS).[3,37]

For the current calculations of CoO the charge transfer effects have not been taken into account, since the states at the start of the L_3 XAS edge as well as the lowest lying final 2p3d RXES states are only little affected by charge transfer effects.[36] The omission of charge transfer effects limits the number of semiempirical parameters: the charge transfer energy Δ, the Hubbard Coulomb repulsion between the 3d electrons U_{dd}, the core hole potential U_{pd}, and the electron hopping parameters can be neglected. The values of the remaining electronic structure parameters used in the interpretation are summarized in Table 1.

Crystal Field Multiplet Calculations for XAS. For our calculations we approximate cobalt to have a formal Co^{2+} valence that can be described effectively by a $2p^63d^7$ configuration. For simulation of the Co $L_{2,3}$-edge all photon-excited dipole-allowed electron transitions from a $2p^63d^n$ initial ground state to a $2p^53d^{n+1}$ excited state are taken into account. Since we consider in RXES the decay process from this excited state, we denominate the $2p^53d^{n+1}$ state to be the intermediate

Table 1. Energetic Values of the Electronic Structure Parameters of CoO Used in the Crystal Field Multiplet Calculations[a]

	initial state	intermediate state	final state
Co^{2+} configuration	$2p^63d^7$	$2p^53d^8$	$2p^63d^8\underline{d}$
F^2_{dd}	8.356	8.925	8.356
F^4_{dd}	5.190	5.550	5.190
F^2_{pd}		5.227	
G^1_{pd}		3.886	
G^3_{pd}		2.210	
ζ_{3d}	0.046	0.058	0.046
ζ_{2p}		9.748	
10Dq	1.050	0.900	1.050
Ds	0.020	0.020	0.020
M	0.010	0.010	0.010
Γ (fwhm)		0.400 (L_3)/0.800 L_2)	0.020
G (fwhm)		0.100	0.100

[a]All energies are in eV.

state in this work. The ground state is affected by 3d spin−orbit coupling, 3d−3d interactions, magnetic superexchange interactions, and crystal field effects. The excited state is furthermore affected by 2p spin−orbit coupling and 2p−3d repulsions. Here the C_4 point group symmetry is used to describe the crystal field with empirical parameters 10Dq, Ds, and superexchange M as indicated in Table 1.[3] Note that the empirical crystal field parameter Dt is 0 eV in all our calculations. The Slater−Condon parameters, used to describe the Coulomb repulsion and exchange interactions, are decreased to 90% of their atomic values (which corresponds to 72% of their Hartree−Fock values) in order to implicitly correct for the effects of charge transfer.[35] The 3d spin−orbit coupling is reduced to 70% of its atomic Hartree−Fock value. The calculations provide the 2p to 3d core level excitations and their oscillator strengths. The discrete transitions are broadened with a Lorentzian function Γ to account for the 2p core hole lifetime broadening. A Gaussian function G, which broadening is set as the experimental resolution, further broadens the spectra. Note that the calculations do not yield absolute energy positions and the resulting spectra are shifted in energy for comparison with the experimental spectra. All XAS spectra were calculated at a temperature of 300 K.

The different states of the initial state configuration $2p^63d^7$ have been labeled in Table 2 in O_h symmetry without 3d spin−orbit coupling, using the following method: starting from the electrostatic matrices given by Griffith[38] for the different terms of the $3d^3$ configuration, electrostatic matrices were constructed for each term of the $3d^7$ configuration (^2E_g, $^2T_{1g}$, $^2T_{2g}$, $^4T_{1g}$, $^2A_{1g}$,$^2A_{2g}$, $^4A_{2g}$,$^4T_{2g}$), using the appropriate changes of phase for the off-diagonal terms and by adding the appropriate crystal field energy to the diagonal part. Then, each matrix (respectively with sizes of 4 × 4, 5 × 5, 5 × 5, 2 × 2, 1 × 1, 1 × 1, 1 × 1, 1 × 1) was numerically diagonalized, yielding the value of the energy (eigenvalue) and the label of each eigenstate for the $3d^7$ configuration. We used the same Racah parameters (A, B, C) and crystal field parameter 10Dq as in the multiplet calculation performed in O_h symmetry without 3d spin−orbit coupling, namely 24.61, 0.112, 0.412, and 1.05 eV respectively. The values of A, B, and C were obtained from those of F^0_{dd}, F^2_{dd}, F^4_{dd} by using the relations given by Cowan:[35] $A = F^0_{dd} - F^4_{dd}/9$, $B = (9F^2_{dd} - 5F^4_{dd})/441$, and $C = 5F^4_{dd}/63$.

Crystal Field Multiplet Calculations for RXES. The inelastic scattering function $F(\Omega,\omega)$ is described by the resonant term of the Kramers−Heisenberg formula[3,39,40] that defines the interference between the X-ray induced electron excitation and subsequent decay processes:

$$F(\Omega,\omega) = \sum_j \left| \sum_i \frac{\langle f|T_2|i\rangle\langle i|T_1|g\rangle}{E_g + \hbar\Omega - E_i + i\Gamma_i} \right|^2 \times \frac{\Gamma_f/2\pi}{(E_g + \hbar\Omega - E_f - \hbar\omega)^2 + \Gamma_f{}^2/4}$$

where $|g\rangle$, $|i\rangle$, and $|f\rangle$ indicate the ground, intermediate, and final state of the probed matter and E_g, E_i, and E_f are the energies. Here $\hbar\Omega$ and $\hbar\omega$ are the energies of the incident and emitted photon. T_1 and T_2 are operators describing the radiative transitions by absorbed and emitted photons, and Γ_i gives the spectral Lorentzian broadening due to the finite time of the core-hole existence in the intermediate state. The second term implies that energy should be conserved in the overall RXES process and that a further Lorentzian broadening Γ_f occurs due the lifetime of the hole in the final state. The RXES spectra for Co^{2+} can be simulated with the crystal field multiplet calculations for the $g = 2p^63d^7 \rightarrow i = 2p^53d^8 \rightarrow f = 2p^63d^8\underline{d}$ transitions. Although the final state $2p^63d^8\underline{d}$ is formally equal to $2p^63d^7$ we use this notation to indicate that the final state still can have a hole in the 3d band, only in an elastic scattering event, where $\hbar\Omega = \hbar\omega$, the final state has no 3d hole (other than the three 3d holes as can be found in the ground state). In the calculations the spectra were broadened by a Lorentzian function accounting for both the intermediate and final state lifetime of the hole and with Gaussian functions accounting for the incident and analyzer experimental resolution. All RXES calculations took the interference effects between the X-ray absorption and emission into account. The shown RXES calculations were all done for the ground state only, which formally relates to a situation at 0 K, except for the Boltzmann-weighted calculations at 300 K as shown in Figure 9. In order to simulate the LH polarized spectra the σ contribution of the light was taken incident on the sample together with the π contribution being detected (in the CTM4XAS program this corresponds to "parallel" incident light plus outgoing "left" light summed with "parallel" incident plus outgoing "right" light). For LV polarized spectra the combination $\pi_{in}-\pi_{out}$ was calculated.

RESULTS AND DISCUSSION

XAS, RXES, and Multiplet Interpretation of CoO. The experimental cobalt $L_{2,3}$ XAS spectra of a CoO reference powder are shown in Figure 1. Both total electron yield (TEY) and total fluorescence yield (TFY) spectra were acquired. These were used to determine the electronic structure parameter values of CoO as given in Table 1 of the Experimental Section for the crystal field multiplet calculations. The crystal field value 10Dq of the ground and final state are set to 1.05 and 0.9 eV respectively. The reduced value of the final state accounts for the crystal field potential reduction due to the 2p core hole.[41] The atomic interactions have been scaled to 90% of their atomic values to effectively include the screening effects of the solid.[35] A small tetragonal distortion is introduced by using a Ds value of 0.02 eV and the 3d spin−orbit coupling is reduced to 70% of its atomic value.

dx.doi.org/10.1021/jp302847h | J. Phys. Chem. C 2012, 116, 15218−15230

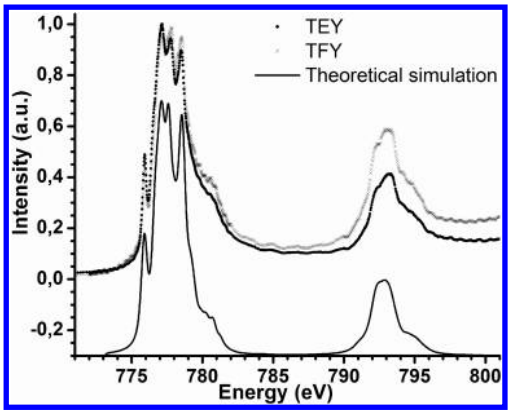

Figure 1. Experimental TEY (dots) and TFY (crosses) cobalt $L_{2,3}$ XAS spectra of a CoO reference powder. The solid line shows the CoO crystal field multiplet calculation.

Superexchange interactions are taken into account with a molecular field of 10 meV. The calculation reproduces the experimental spectra adequately.

Next the XAS and RXES spectra of the cobalt oxide single crystal and nanocrystals were acquired. Figure 2 shows a TEM image of the studied CoO nanocrystals as further characterized in Figure S1 of the Supporting Information. The particles are spherical and monodisperse with an average diameter of 4.2 nm and a polydispersity of 12% (defined as the standard deviation over the average of the particle diameter). Using geometric considerations and a fcc CoO crystal structure with unit cell dimensions $a = b = c = 0.426$ nm we estimate that approximately 15% of the atoms is part of the surface of the nanocrystals.[42] More details on the estimation can be found in the Supporting Information.

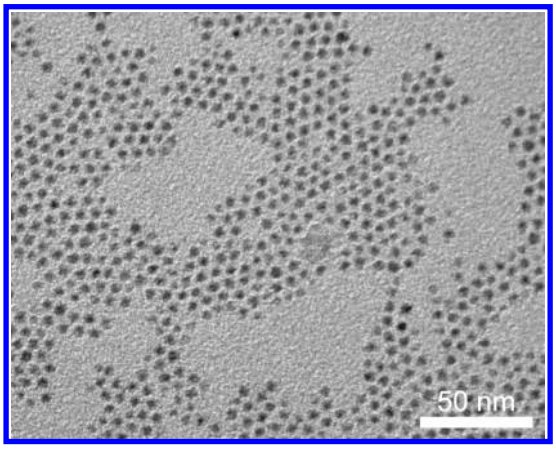

Figure 2. TEM image of 4.2 ± 0.5 nm ε-Co/CoO nanoparticles (the ± sign indicates the standard deviation in the particle diameter).

Figure 3 shows the cobalt $L_{2,3}$ XAS edge and five cobalt 2p3d RXES spectra of the materials. The shown RXES spectra were acquired in the linear horizontal (LH) polarized geometry and the spectra were taken at fixed excitation energies (denoted *a*–*e* in the remainder of the text) for both the nanocrystals and the single crystal. A difference is that the nanocrystals data were acquired at 291 ± 5 K, while single crystal data were taken at 10 K. The XAS spectrum of the CoO nanoparticles is almost identical with the CoO powder spectrum, while that of the CoO single crystal has an altered fine structure. This XAS spectrum is a TFY spectrum and the unusual branching ratio of ∼1, the ratio between the L_3 and L_2 XAS edge, indicates that this spectrum is suffering from saturation/self-absorption effects.[43] However, it is shown in order to indicate the excitation energies of the RXES spectra, which themselves are not visibly affected by self-absorption effects. The resonant X-ray emission spectra are depicted in the bottom panels of Figure 3, parts a and b. 2p3d RXES at the cobalt *L*-edge probes among other things the 3d–3d, charge transfer (ligand-to-metal or metal-to-ligand), and charge fluctuation (metal-to-metal) excitations. The energies of the spectroscopic features in the RXES spectra at excitation energy *c* and *d* are listed in Table 2. Most spectral features are intense d–d excitations since these are allowed in RXES. The main d–d excitations are interpreted on a full RXES calculation, including the splitting of these states due to the more subtle tetragonal distortion, 3d spin–orbit coupling, and superexchange as will be discussed later. In the final two columns of Table 2 the d–d excitations are interpreted based on a calculation that only includes the CoO atomic multiplet octahedral field parameters. Although this is an incomplete representation, and valence spin–orbit coupling will also mix the states, we have labeled most d–d

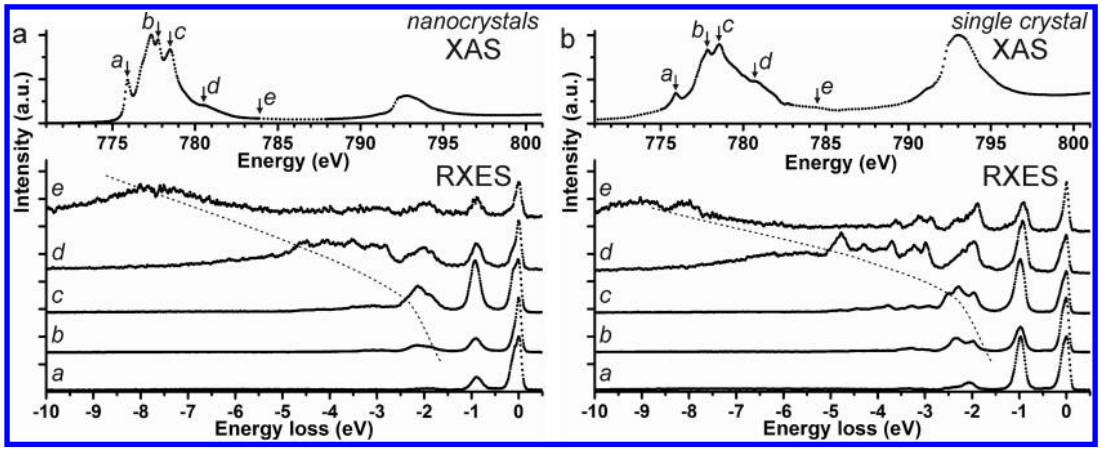

Figure 3. Cobalt $L_{2,3}$ XAS (top panels) and 2p3d RXES spectra (bottom panels) for (a) CoO nanocrystals at 291 K and (b) a CoO single crystal at 10 K. The RXES spectra were acquired at five fixed excitation energies labeled *a*–*e* and this denomination will be used in the remainder of the text. The shown spectra were all acquired in the linear horizontal (LH) polarized geometry. The dashed, curved lines in the RXES panels indicate the position of transitions caused by resonant X-ray fluorescence and resonating charge-transfer transitions as discussed in the text.

dx.doi.org/10.1021/jp302847h | J. Phys. Chem. C 2012, 116, 15218–15230

Table 2. Energies of the Experimental CoO Spectroscopic RXES Features in Nanocrystals and a Single Crystal at Excitation Energies *c* and *d*, Together with Energies at *c* for the Crystal Field Multiplet Interpretation As Discussed in the Text[a]

spectroscopic feature	nanocrystals at *c*	nanocrystals at *d*	single crystal at *c*	single crystal at *d*	RXES calculation at *c*	calculated energies and assignment[b] in O_h without ζ_{3d}	
shoulder	0.10	0.13	0.08	0.10	0.07	0	$^4T_{1g}(^4F)$
peak	0.92	0.88	0.98	0.93	0.98	0.91 + 0.98	$^4T_{2g}(^4F)$ + $^2E_g(^2G)$
shoulder	1.87	1.85	1.96	1.97	1.89 + 2.00	1.83 + 1.86 + 1.96	$^2T_{1g}(^2G)$ + $^2T_{2g}(^2G)$ + $^4A_{2g}(^4F)$
peak + shoulder	2.13	1.99	2.28 + 2.36	2.04	2.42	2.41 + 2.45	$^2T_{1g}(^2H)$ + $^4T_{1g}(^4P)$
peak			2.50	2.20	2.61	2.60	$^2A_{1g}(^2G)$
peak		2.8	2.90	2.98	2.93	2.87 + 3.03	$^2T_{2g}$ + $^2T_{1g}$
peak		3.1	3.27	3.23	3.09	3.24	^2E_g
peak		3.5	3.78	3.70	3.67	3.61 + 3.76 + 3.85	$^2T_{2g}$ + $^2T_{1g}$ + ^2E_g
peak		4.1		4.29	4.58	4.50	$^2T_{2g}(^2F)$
peak		4.5		4.77	4.90	4.82 + 4.83	$^2T_{1g}(^2F)$ + $^2A_{2g}(^2F)$
						7.04	^2E_g (^2_bD)
						7.11	$^2T_{2g}$ (^2_bD)

[a]All energies are in eV. [b]The states are indicated with O_h symmetry labels and their atomic multiplet origin is shown between brackets. It must be noted that the symmetry labeled states intermix and that the atomic labeling is used mainly for a convenient terminology. Symmetry labeled states that are not directly linked to their atomic origin are the $^2T_{1g}(^2P)$, $^2T_{1g}(^2H)$, $^2E_g(^2H)$, $^2T_{2g}(^2H)$, $^2T_{2g}(^2_aD)$, and $^2E_g(^2_aD)$ levels since these doublet states mix strongly.

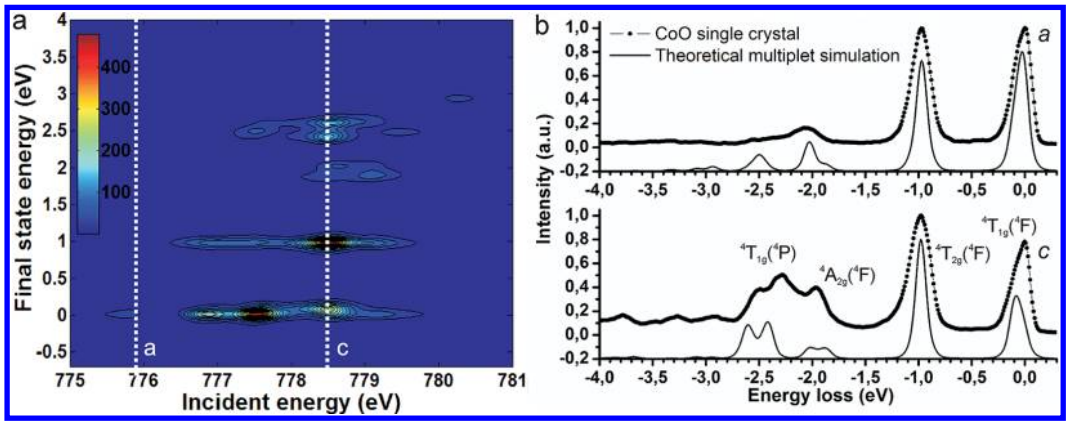

Figure 4. (a) Crystal field multiplet 2p3d cobalt two-dimensional RXES plane simulation of cobalt(II) in CoO. The white dotted line corresponds to the excitation energy *a* and *c* as shown in Figure 3. (b) The experimental, linear horizontal polarized spectra of the CoO single crystal at these energies are shown (dots + line) together with the crystal field multiplet spectra with the same polarization (solid lines).

excitations with octahedral symmetry labels in order to account for a rough energetic classification.[44] In Table 2 it is important to note that the broadening of the elastic peak at 0 eV, with a maximum around approximately 100 meV, is visible for most excitation energies and caused by the $^4T_{1g}(^4F)$ ground state manifold. The peak around 1 eV is due to excitations to the $^4T_{2g}(^4F)$ states, the shoulder around 1.9 eV due to transitions to the $^4A_{2g}(^4F)$ states, and the manifold of peaks around 2−2.5 eV due to transitions to, among others, the $^4T_{1g}(^4P)$ states. In a pure octahedral symmetry the crystal field value 10Dq would be given as the energy difference between the $^4T_{2g}(^4F)$ and the $^4A_{2g}(^4F)$ states, and not by the energy difference between $^4T_{1g}(^4F)$ and $^4T_{2g}(^4F)$ as $^4T_{1g}(^4F)$ is hybridized with the $^4T_{1g}(^4P)$ states.[44,45] This yields for the nanocrystals and the single crystal an average 10Dq of 0.96 and 1.01 eV, respectively, although the situation is further complicated by peak shifting as a result of the tetragonal distortion, 3d spin−orbit coupling, and superexchange. It must also be noted that the exact position of the peaks with respect to the peak at 0 eV is not constant for varying excitation energies as shown in Table 2. Overall the experimentally determined 10Dq values of ∼1 eV are close to the value of 1.05 eV as used for the $3d^7$ state in the crystal field calculations (given in Table 1). The Racah parameter *B* can be estimated from $B = (9F^2_{dd} - 5F^4_{dd})/441 = 900\ cm^{-1}$,[35] and in pure octahedral symmetry the energy difference between the ^4F and ^4P levels is given by 10Dq = 15*B*.

dx.doi.org/10.1021/jp302847h | J. Phys. Chem. C 2012, 116, 15218−15230

For 10Dq = 1.05 eV the parameter indeed results in B = 900 cm^{-1}, which gives a nephelauxetic ratio β = 0.93 (the free ion value of B = 971 cm^{-1} for Co^{2+}).[46] Furthermore, next to excitations that occur at a fixed energy loss, such as transitions to d−d and phonon excitations that are present in the final state, peaks occur at a varying energy loss but at fixed emission energy.[47] Fixed emission energy peaks originate from emission to a final state that maintains part of the excitation as present in the intermediate state. Examples are a charge transfer excitation, or an electron excited to a "free" state as present in the intermediate state, which are maintained in the final state. For example, a charge transfer excitation to a band in the intermediate state can have a fixed emission energy over the width of this band.[48,49] It was suggested[25,48] that the structure appearing at an energy loss of ∼8 eV in the RXES spectrum of CoO recorded at energy *e* is mostly due to charge-transfer transitions based on calculations which include these effects. This peak is not calculated in the present crystal field multiplet simulations.

Figure 4 shows the crystal field multiplet calculated cobalt 2p3d RXES spectra using the same parameters as given in Table 1 and used for the 2p XAS calculation in Figure 1. A calculation for the $2p^63d^7 \rightarrow 2p^53d^8 \rightarrow 2p^63d^8\underline{d}$ transitions yields the full RXES plane as shown in Figure 4a. This two-dimensional plot shows the lost or transferred energy as a function of the excitation energy over the cobalt L_3 XAS edge. Figure 4b shows the experimental RXES spectra acquired on the CoO single crystal at excitation energies *a* and *c*, along with the calculated CoO spectra at the same excitation energy. The energies and origins of the relevant transitions are also given in Table 2. Around 2.2 eV the calculations do not reproduce the experimental spectra well. This is because (a) charge transfer excitations and (b) X-ray fluorescence from the low-energy side of the L_3-edge are not calculated here. The former occur around this energy in CoO,[14] and the latter contribute for these energies at excitation energy *c*. Furthermore the peaks above 2.5 eV are not further interpreted in this work since the focus in the current study is on the $^4T_{1g}(^4F)$ ground state manifold. It must be noted, however, that due to the occurrence of much more intense charge transfer excitations in this regime in optical absorption spectroscopy, RXES actually allows for a unique study of these excitations. We also note that the first peak, which we put at 0 eV in our analysis, is complex. In the experiment elastic scattering channels that are not material-specific are present. This peak is shown in Figure S2a in the Supporting Information acquired on a carbon reference sample at excitation energy *a* together with an experimental spectrum at the same excitation energy for cobalt monoxide. The cobalt monoxide spectrum shows a peak and a shoulder. Calculations of the material specific contributions are shown in Figure S2b in the Supporting Information for excitation energy *a*−*e* and reveal that the peak maximum is energy dependent and that it occurs at low energy (nonzero) loss values. The shoulder of the experimental cobalt monoxide peak is thus interpreted as originating from tetragonal distortions, 3d spin−orbit coupling, and superexchange interactions within the cobalt monoxide as will be discussed later. The energy of the entangled nonmaterial specific elastic line and low energy material specific transitions are calibrated with respect to the elastic line on the carbon reference sample. The good match between the experiment and theory for the energies of the other d−d excitations validates this approach and overall the spectra are well simulated by the calculations.

Upper Limit of the Cobalt 3d Hole Lifetime Broadening in CoO. Comparisons of the experimental and theoretical RXES spectra are here used to estimate the upper limit of the lifetime broadening due to the 3d hole in the RXES final state. Figure 5 shows the linear horizontal polarized

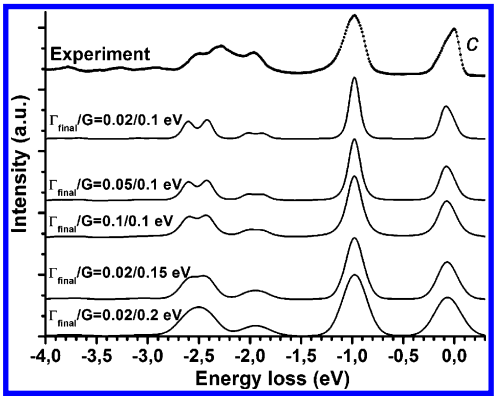

Figure 5. Experimental linear horizontal polarized RXES spectrum at excitation energy *c* acquired on the CoO single crystal (dots + line; top) and theoretical crystal field multiplet spectra at the same excitation energy *c*. Several final state Lorentzian (Γ_{final}) and Gaussian (G) functions were chosen, with varying fwhm, to broaden the theoretical spectra (the intermediate and final state Gaussian functions are varied simultaneously). The fwhm values are indicated in eV.

experimental spectrum taken at excitation energy *c* on the CoO single crystal and several theoretical spectra with different broadenings. The fwhm of the final state Lorentzian and Gaussian functions that are used to account for the 3d hole lifetime and the experimental setup broadening, respectively, are varied systematically. The intermediate and final state Gaussian functions are varied simultaneously with the same value. The Lorentzian accounting for the intermediate state broadening is determined by the 2p core hole lifetime and is fixed at 0.4 eV in all calculations. The final state Lorentzian and Gaussian broadenings must be ≤0.1 eV to allow enough fine structure to occur in the simulations in order to reproduce the experiment. The calculations in the rest of this work were allowed to be slightly more detailed than the experiment and a final state Lorentzian function with a 0.02 eV fwhm and Gaussian functions with a 0.1 eV fwhm were chosen. The upper limit of the lifetime broadening of the 3d hole final state in CoO is thus determined to be 0.1 eV, but it must be noted that the 3d hole lifetime is probably dependent on the crystal symmetry and might thus be different for Co^{2+} in other compounds.

The Influence of Tetragonal Distortion, 3d Spin−Orbit Coupling, and Magnetic Excitations. Due to the unprecedented spectral resolution of the ADRESS beamline, being ≤100 meV at the Co *L*-edge, we see additional structure in the elastic peak at 0 eV of the RXES spectra as shown in Figure 3. Figure 6a shows the electronic structure description of this ground state manifold considering atomic multiplet, crystal field, 3d spin−orbit coupling, and magnetic superexchange effects. In spherical symmetry (SO_3) the 28-fold degenerate ^4F multiplet state is the ground state. In an octahedral field (10Dq = 1.05 eV) this manifold is branched and the 12-fold degenerate $^4T_{1g}(^4F)$ state forms the ground state. Application of the tetragonal distortion (Ds = 0.02 eV) lowers the symmetry and branches the state to $^4A_2$ and ^4E states. This gives rise to the ^4E excited states within 100 meV of the $^4A_2$

dx.doi.org/10.1021/jp302847h | J. Phys. Chem. C 2012, 116, 15218−15230

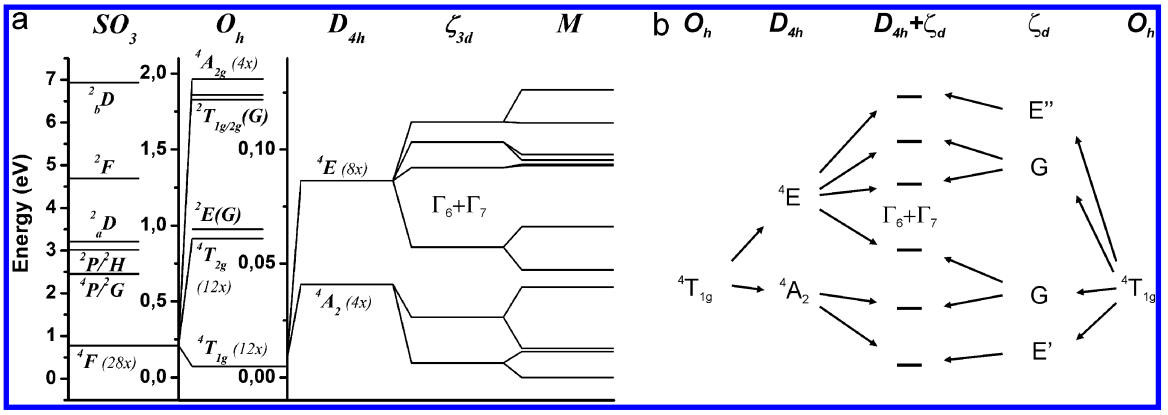

Figure 6. (a) Branching of the Co^{2+} energy levels in spherical SO_3 symmetry due to atomic multiplet effects (left), an octahedral O_h crystal field (middle), a tetragonal D_{4h} distortion, the 3d spin−orbit ζ_{3d} coupling and the superexchange M. (b) Current branching scheme and alternative branching scheme, where the 3d spin−orbit coupling is considered first, lead to the same final states. For $T > T_N$ the splitting might end after inclusion of the 3d spin−orbit coupling since the presence of a tetragonal distortion and superexchange interaction are reported to occur below T_N.

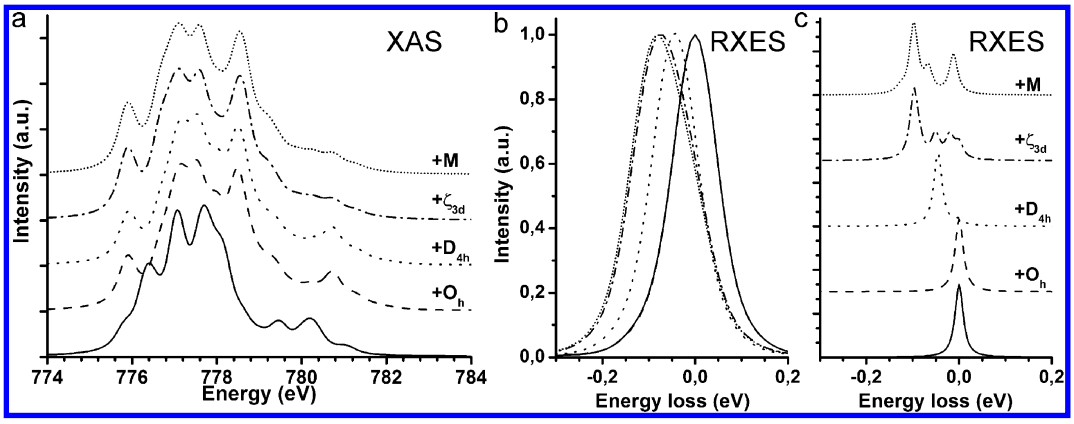

Figure 7. Theoretical calculation of multiple electronic interaction on (a) the 2p XAS and (b, c) the 2p3d RXES spectra of CoO. The Gaussian functions accounting for experimental broadening have a fwhm of (b) 100 and (c) 5 meV. The solid line shows the spectrum of a Co^{2+} ion in spherical SO_3 symmetry, the dashed line in octahedral O_h symmetry, the long dotted line shows the effect of including a small tetragonal D_{4h} distortion, the dot−dash line includes 3d spin−orbit ζ_{3d} coupling and the short dotted line shows the effect of including the magnetic superexchange interaction M.

ground state. The states split further to Γ_6 and Γ_7 states[50] under the influence of the 3d spin−orbit coupling (46 meV) and the superexchange (10 meV), giving rise to a series of levels within 120 meV above the ground state. Since the CoO single crystal data were taken below T_N (at 10 K) the presence of the three effects is likely since tetragonal distortions and superexchange have been observed in the antiferromagnetic CoO phase.[11] The nanocrystals data were acquired around T_N (291 ± 5 K) and the presence of a tetragonal distortion and superexchange is unclear. Figure 6b shows the current branching scheme and an alternative branching of the $^4T_{1g}(^4F)$ state if 3d spin−orbit coupling is considered before the tetragonal distortion. The splitting due to the 3d spin−orbit coupling alone also gives rise to peaks within the first 100−150 meV of the ground state being the $E'(J = 1/2)$, $G(J = 3/2)$, $G(J = 5/2)$, and $E''(J = 5/2)$ states.[18] This approach clearly shows that the splitting of the ground state can be influenced by all three effects, where we add that further phonon-induced splitting is not considered here.

We further note that if the 12 Γ_6 and Γ_7 states are analyzed as consisting of multiple single particle states, the $t_{2g}^{\uparrow}3\ e_g^{\uparrow}2\ t_{2g}^{\downarrow}2$ state makes up 90% of the manifold, the other 10% divided over a range of other contributions that are mixed by the 3d spin−orbit coupling. Due to the tetragonal distortion there is an imbalance between the $t_{2g} > e_g$ states and the $t_{2g} > b_{2g}$ states. The combined effect of the 3d spin−orbit coupling, the tetragonal distortion, and the superexchange leads to a lowest energy configuration that contains 50% the $a_1^{\downarrow}\ b_1^{\downarrow}\ b_2^{\downarrow}$ hole state and 41% the $a_1^{\downarrow}\ b_1^{\downarrow}\ e^{\downarrow}$ hole state. The remaining 10% are divided over a number of other states. The first excited state has similar character and the second excited state is more pure in its $a_1^{\downarrow}\ b_1^{\downarrow}\ b_2^{\downarrow}$ hole character. This analysis shows that the Γ_6 and Γ_7 states are a complex mixture of three-hole states that cannot be simplified within a single particle interpretation.

Figure 7 shows the effect of the crystal field, 3d spin−orbit coupling, and superexchange on the structure and position of the 2p XAS spectra and the ground state RXES manifold in the calculations. These same effects are applied in Figure 7a−c, but in the RXES spectra shown in parts b and c of Figure 7 the Gaussian broadening functions have a fwhm of 100 and 5 meV, respectively (the final state Lorentzian function has a fwhm of 20 meV). The broadening in Figure 7b is representative for the current resolution at the ADRESS beamline, while the resolution in Figure 7c shows what would be possibly observable with a 20 times increased experimental resolution, provided the lifetime broadening is correct. In a perfect spherical or octahedral field the elastic RXES peak has its maximum at 0 eV exactly, if the 3d spin−orbit coupling and

dx.doi.org/10.1021/jp302847h | J. Phys. Chem. C 2012, 116, 15218−15230

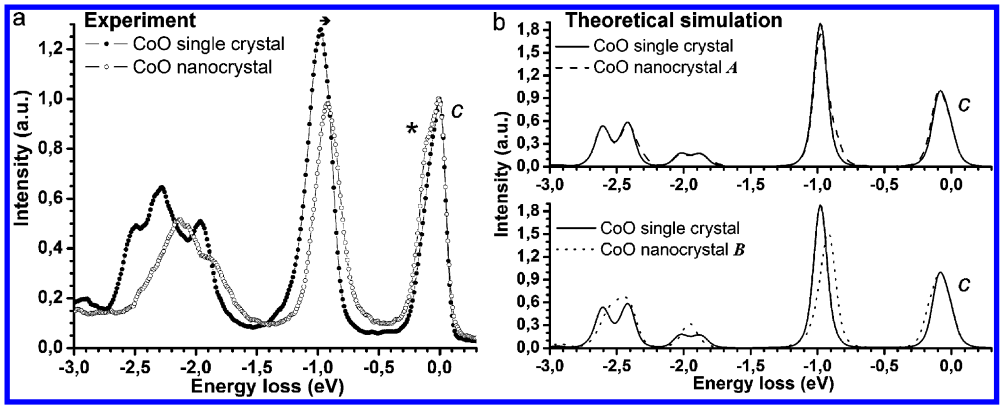

Figure 8. Experimental RXES spectra at excitation energy *c* in the CoO single crystal (solid dots) and nanocrystals (open dots). The $^4T_{2g}(^4F)$-based peak at 0.98 eV is shifted down to 0.92 eV in the nanocrystals (indicated by the arrow). The elastic peak at 0 eV is broadened to a larger extent in the nanocrystals as indicated by the asterisk. Note that the single crystal data were acquired at 10 K and the nanocrystal data at 291 ± 5 K. (b) Calculated RXES spectra at the same energy for the single crystal (black solid line; shown in top and bottom panels) and for the two nanocrystal calculations ***A*** (dashed line; top) and ***B*** (dotted line; bottom) as discussed in the text.

superexchange are both zero. The difference between a spherical and octahedral field is large in the 2p XAS spectra shown in Figure 7a. Inclusion of a small tetragonal distortion has little influence on the XAS spectrum, but broadens and shifts the quasi-elastic RXES peak to higher loss energies due to the above-described splitting of the ground state. The disappearance of the pure elastic peak at 0 eV is known for systems with a D_{4h} symmetry studied with linear horizontally polarized light as, for example, shown for the copper ion in La_2CuO_4.[51] This splitting is observable with a better theoretical resolution as shown in Figure 7c. Inclusion of the 3d spin−orbit coupling has some effect on the 2p XAS spectrum, while the superexchange at the current strength has a small effect. Both effects broaden the elastic RXES peak even further and shift it to higher transferred energy due to the further splitting of the ground state level as visible in Figure 7b,c. Overall, 2p XAS is sensitive to some of the presented effects, but the 2p3d RXES spectra are much more sensitive to them. To comprehend this one must realize that only the elastic peak of the RXES spectrum at one excitation energy has been considered in this comparison. If the full spectra at different excitation energies are considered RXES contains a multitude of information to determine the strength of the electronic structure parameters. With the current resolution, however, the exact strengths of these interactions are hard to determine from RXES alone, since the combination of tetragonal distortion, 3d spin−orbit coupling, and superexchange effects make it difficult to disentangle the $^4T_{1g}(^4F)$-derived manifold around 0 eV.

CoO Single Crystal versus Nanocrystals. The RXES spectra of the ε-Co/CoO nanoparticles and the CoO single crystal are clearly different and the energies of their spectroscopic features were given in Table 2. Here the spectra acquired at excitation energy *c* are shown in Figure 8a and compared in detail. The d−d excitations around 1 and 2−2.5 eV are shifted to lower energies in the case of the nanocrystals. The $^4T_{2g}(^4F)$-branched peak has its maximum at 0.98 eV in case of the single crystal, but it occurs at 0.92 eV for the nanocrystals. This indicates that the effective crystal field is smaller in the nanoparticles and if the influence of tetragonal, spin−orbit, and superexchange effects is neglected we get experimental 10Dq values of 0.96 and 1.01 eV for the nanocrystals and single crystal, respectively, as discussed earlier. Furthermore, the shoulder of the elastic peak at approximately 100 meV is more pronounced in the case of the nanoparticles.

The origin of the observed differences is addressed in Figure 8b, as well as in Figure S3 in the Supporting Information. The surface of the nanocrystals contains approximately 15% of the cobalt ions as discussed in the Supporting Information. Cobalt ions in the surface of a CoO nanocrystal will likely have a coordination number <6 and a lower site symmetry than their octahedral symmetry in the CoO bulk phase. Two sets of crystal field multiplet RXES calculations were made at excitation energy *c* for Co^{2+} ions possessing a lower symmetry and these are shown in Figure S3 in the Supporting Information. In the first set the value of the parameter Ds was increased from 0.02 to 0.05, 0.1, and 0.2 eV. In the second set the value of Ds was increased and fixed to 0.05 eV, while the value of the parameter 10Dq was lowered, both in the initial and intermediate transition RXES state. The increase of Ds and lowering of 10Dq lowered the Co^{2+} ion symmetry from octahedral to tetragonal. In order to mimic the nanocrystal spectra 15% of the low-symmetry spectra, representing cobalt ions in the nanoparticle surface, were added to 85% of the single crystal bulk calculations. From the comparison of these spectra with the experimental ones, the best match using this approach is found for the low-symmetry calculation with Ds = 0.05 eV and $10Dq_{initial}/10Dq_{intermediate}$ = 0.9/0.75 eV. The corresponding spectrum is in the top panel of Figure 8b indicated as CoO nanocrystal ***A***. Alternatively, both experimental differences between the single and nanocrystals, as shown in Figure 8a, can be explained by an increased superexchange coupling *M* that has been shown to occur for CoO surfaces,[52] noting that the nanocrystals have a much larger surface area per volume than the single crystal. One could also hypothesize that a larger Co−O average distance in the CoO nanoparticles would yield a weaker crystal field and result in the lowering of the d−d excitation energies, but this does not explain the broadened $^4T_{1g}(^4F)$ ground state manifold. A calculation that uses the same electronic structure parameters as shown in Table 1, but with an increased value of *M* of 40 meV and a decreased value of $10Dq_{initial}/10Dq_{intermediate}$ of 1.0/0.85 eV, is shown as the CoO nanocrystal calculation ***B*** in the lower panel of Figure 8b. The latter calculation mimics the experimental nanocrystal spectrum better and based on this we ascribed the observed differences for the single crystal and

dx.doi.org/10.1021/jp302847h | J. Phys. Chem. C 2012, 116, 15218−15230

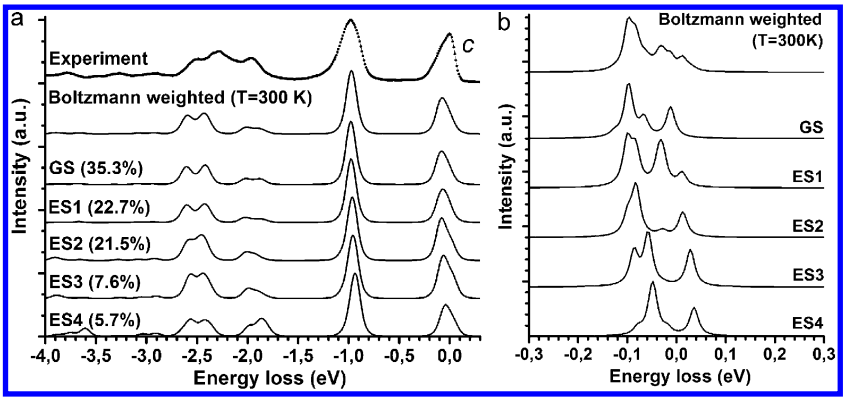

Figure 9. (a) Experimental linear horizontal polarized RXES spectrum at excitation energy *c* in the CoO single crystal (dots + line; top) together with the calculated spectra at this energy and polarization of the ground state and the first four excited states (indicated as ES1−4). Their spectral weight at 300 K is indicated between brackets and applies equally to panel b. The Boltzmann weighted spectrum is shown. (b) The same calculations as shown in panel a, but now broadened with Gaussian functions having a fwhm of 5 meV instead of 100 meV. The excited states exhibit spectral anti-Stokes contributions.

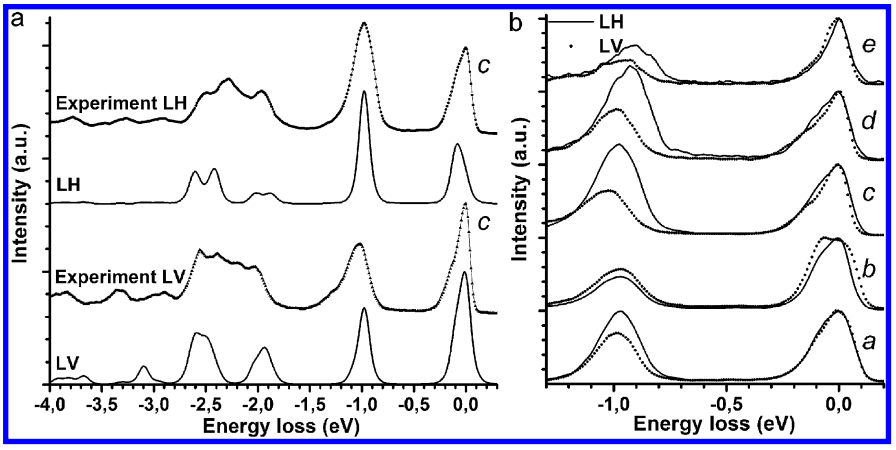

Figure 10. (a) Experimental RXES spectra (dots + line) acquired on the CoO single crystal with linear horizontal (LH) and linear vertical (LV) polarized light. The crystal field multiplet calculations for the separate LH and LV polarizations are shown. (b) Experimental RXES spectra acquired on the CoO single crystal at excitation energy *a*−*e* with LH (solid line) and LV (dots) polarized light.

nanocrystals to an effectively larger average Co−O distance and to a possibly increased magnetic exchange. It should be noted that in these calculations more complicated effects, including a possible nonstoichiometry between Co and O in the surface, the type of surface defect states, and their influence on the RXES spectra are not considered. Dedicated surface science, X-ray scattering, and high-resolution spectromicroscopic[53,54] experiments might be designed to study the nanocrystal effects in more detail. In the next section we discuss what the additional effects on the RXES spectra could be of the different temperatures at which the spectra were acquired (10 K for the single crystal versus 291 ± 5 K for the nanocrystals).

Temperature Dependency of CoO RXES Spectra. The CoO RXES spectral shape is a function of the temperature-dependent occupation of excited states and phonon modes. The consequence of having 12 excited states within the first 100−150 meV above the ground state is that spectra acquired at room temperature will likely have non-negligible spectral weight from these excited states. Here, the energies of the first 12 states were calculated and weighted according to a Boltzmann function (occupied fraction $p_i = \exp[-\Delta E_i/k_bT)/\sum_j \exp(-\Delta E_j/k_bT]$, with k_b being the Boltzmann constant), using a temperature of 300 K. It was found that the first five states, including the ground state, account for 93% of the spectral weight. At 10 K the ground state is populated for 99.9998%. The RXES spectra of the excited states at excitation energy *c* are shown in Figure 9a, together with their Boltzmann weighted spectrum at 300 K. The ground state and Boltzmann weighted spectrum are highly similar and both mimic the experimental spectrum well. Figure 9b shows the effect of inclusion of the excited states on the spectral shape of the ground state $^4T_{1g}(^4F)$ manifold. Both Gaussian broadening functions used have a fwhm of 5 meV (the intermediate and final state Lorentzian functions have a fwhm of 0.4 and 0.02 eV, respectively). With this 20 times improved experimental resolution, as compared to the current situation, the Boltzmann weighted spectrum at 300 K does appear different from the ground state spectrum alone. Also, at higher excited states the $^4T_{1g}(^4F)$ states occur at lower loss energies and an anti-Stokes feature is present. At high temperatures and with improved experimental resolution it might be possible to measure such contributions in the CoO RXES spectra in future experiments.

The effects of temperature-dependent phonon modes should also be considered, although the localized character of the CFM model does not allow their inclusion in the calculations. It is known from infrared[16] and neutron scattering[19] studies that transverse and longitudinal optical modes exist around 42 and 65−70 meV and that these split in multiple states with an

dx.doi.org/10.1021/jp302847h | J. Phys. Chem. C 2012, 116, 15218−15230

energy difference of 2 meV below the Néel temperature T_N of ca. 290 K. Electron energy loss spectroscopy (EELS) experiments[20] on CoO(100) planes have revealed phonon modes at 65 meV (plus weak modes above 100 meV) and relatively less intense surface modes at 45 and 50 meV. The low energy of the phonon modes make them experimentally unresolvable and they contribute thus to the intensity of the elastic peak and the shoulder attributed here to the 12 $^4T_{1g}(^4F)$ states. In general the overall phonon scattering intensity is minimized at the *L*-edge compared to the *K*-edge.[47] The phonon transition probability is expected to be smaller than resonant elastic scattering events or pure d−d excitations that are fully dipole allowed in RXES. Upon increasing temperatures phonon modes become more intense and increasingly mix with electronic excitations.[16] This will tend to shift the overall peak at 0 eV to somewhat higher energies, counteracting the effect of populating more excited states as discussed above.

In the CoO nanocrystal data, which were acquired at 291 ± 5 K as compared to the single crystal data acquired at 10 K, the $^4T_{1g}(^4F)$ manifold was broader and occurring at higher energy losses than in the single crystal data. In the previous section we attributed the broadening of the $^4T_{1g}(^4F)$ manifold to an increased magnetic exchange. The here presented discussion on the population of anti-Stokes peaks and phonon-mixing upon increasing the temperature leaves room for an additional explanation of the observed $^4T_{1g}(^4F)$ manifold. We conclude that it would be a very interesting experiment to perform temperature-dependent RXES experiments with the highest possible energy resolution to reveal the interplay between phonons, spin−orbit, and (magnetic) exchange interactions in more detail.

Polarization Dependency of CoO RXES Spectra. Figure 10a shows the polarization dependence of the experimental RXES spectra taken from the CoO single crystal at excitation energy *c*. The calculations with LH and LV combinations reproduce the experimental CoO single crystal spectra. In general, the experimental linear vertical polarized spectra show a larger spectral weight at the high-energy-loss end of the 2 eV manifold as compared to the linear horizontal polarized spectra. This is reproduced by the calculations. Also the intensity ratio between the elastic peak at approximately 0 eV and the peak at approximately 1 eV is well reproduced by the calculations for both the vertical and horizontal linear polarizations. The full 2p3d crystal field multiplet calculated cobalt 2p3d RXES plane for the LV polarized geometry is given in Figure S4 of the Supporting Information. Figure 10b shows part of the experimental spectra at excitation energies *a*−*e* acquired in the linear vertical and linear horizontal polarized geometry. The ground state manifold is a function of the scattering geometry (momentum dispersion dependent), of the light polarization, and of the excitation energy. The experimental spectra in Figure 10b reveal this dependence on light polarization and excitation energy, since the broadness of the RXES peaks and the relative energy difference between them varies as a function of these degrees of freedom.

Discussion on the 2p3d RXES and Crystal Field Multiplet Obtained Parameters. The crystal field multiplet input values found in this study describe the electronic structure of cobalt(II) oxide and are benchmarked here against literature results. CoO 2p3d RXES spectra were acquired previously by Magnuson et al.[25] and Chiuzbăian et al.[26] and interpreted by using multiplet calculations that included charge transfer excitations (which has not been done here). The 10Dq values used in previous interpretations including charge transfer (0.5−0.7 eV)[12,25] are lower compared to values from infrared and optical spectroscopy studies[13−15] that apply crystal field theory without charge transfer and compared to the value used in this study. In models without charge transfer the 10Dq parameter has to compensate for the metal−ligand hybridization effects, which typically increases 10Dq by approximately 0.3 eV for divalent metal oxides (see, for example, Hu et al.[55]). An additional effect on the 10Dq value in X-ray studies is that the core hole decreases 10Dq.[41] In the case of CoO, 10Dq is 1.05 eV in the initial and 0.9 eV in the intermediate state when the 2p core hole is present.

The $^4T_{1g}(^4F)$ ground state manifold of CoO was interpreted here on the basis of a tetragonal distortion, 3d spin−orbit coupling, and magnetic excitations. We used Ds = 0.02 eV, 3d ζ_{3d} = 0.046 eV, and *M* = 0.01 eV to account for these effects. The splitting of this state has been measured as early as 1959 with infrared spectroscopy and with a better resolution as presented here and interpreted on the basis of 3d spin−orbit coupling.[15] The states have recently been revisited by infrared spectroscopy and interpreted on the basis of a tetragonal distortion, 3d spin−orbit coupling, and magnetic excitations.[16] The tetragonal distortion crystal field parameter *D* was determined to be −47.8 cm^{-1}, the spin−orbit coupling λ was −151.1 cm^{-1}, and the superexchange constant *J* was 17.5 cm^{-1}. If we transfer our parameters to the model as used by Kant et al. (as far as possible), we find similar values of *D* = −44.3 cm^{-1}, λ = −124 cm^{-1}, and *J* = 13.4 cm^{-1}.[16,19,56,57] As stated before, the 3d spin−orbit coupling value was reduced in this study to 70% of its free Co^{2+} ion value. For 3d transition metal ions with a $3d^1$, $3d^2$, high-spin $3d^6$, or high-spin $3d^7$ configuration reduced 3d spin−orbit coupling values have been observed previously, for example, in CrO_2 and Fe_2SiO_4 where the 3d spin−orbit coupling is quenched.[3] For several Co^{2+}-bearing compounds there is experimental evidence that the 3d spin−orbit coupling is significantly reduced. In $CoCl_2$ its value is, for example, λ = −140 cm^{-1},[45] as compared to the free ion value of λ = −180 cm^{-1} according to Newman et al.[15] or λ = −177 cm^{-1} as used here. For Co^{2+} in CoO some previous calculations have used unquenched 3d spin−orbit coupling values, but other studies also found reduced 3d spin−orbit coupling values that correspond to 40%[19] or ∼80%[16] of the ionic value. The reason that previous $L_{2,3}$ XAS calculations for CoO used ionic values is that $L_{2,3}$ XAS does not discriminate very well between the ionic value and 70% of that value (as illustrated, for example, in Figure 7a). The high-resolution 2p3d RXES data, however, allow for the determination of the reduction of the 3d spin−orbit coupling, because the 12 excited $^4T_{1g}(^4F)$ states would possess an energy that is too high if an unquenched ionic 3d spin−orbit coupling is used. We attribute the physical meaning of the reduction of the 3d spin−orbit coupling to (1) the effect of the symmetry reduction from octahedral symmetry, (2) the effect of charge transfer, and (3) the effects due to translation symmetry (band effects). These combined effects can be simulated with a reduced 3d spin−orbit coupling in the crystal field multiplet calculations. Overall the here presented interpretation does reproduce the experimental 2p XAS and 2p3d RXES results well, and furthermore it is also able to explain 1s XAS spectra and 1s2p RXES spectra of CoO as described by Kurian et al.[58]

Finally, the current experimental resolution of the RXES spectra thus clearly shows the presence of an approximately 0.1 eV broad ground state manifold, but it does not allow yet for a

careful disentanglement of its origin. In this light, our results should be regarded as the first observation of these states with RXES and a tentative indication of the factors that play a role in their splitting.

SUMMARY AND CONCLUSIONS

CoO nanocrystal and single crystal 2p XAS data were experimentally acquired together with 2p3d RXES data. The RXES data have a record spectral resolution compared to other CoO RXES data, and allow a peak fwhm of approximately 0.1 eV. The data were interpreted with 2p XAS and 2p3d RXES crystal field multiplet calculations with an optical 10Dq value of 1.05 eV and it was found that the ground state levels at 0 eV are broadened by tetragonal distortions, 3d spin−orbit coupling, and magnetic superexchange interactions. The parameters accounting for these effects had strengths of Ds = 0.02 eV, ζ_{3d} = 0.046 eV, and M = 0.01 eV, respectively. The upper limit of the natural line width resulting from the finite 3d hole lifetime was determined to be ≤0.1 eV, implying that the resolution in the present data is still setup limited. The calculations address the origin of the different observed d−d excitations and these were labeled according to their symmetry. From this interpretation we are able to determine experimental 10Dq values of 0.96 and 1.01 eV for the nanocrystals and the single crystal respectively assuming a perfect octahedral symmetry (which is not the case). We further showed that 2p XAS is sensitive to the octahedral field and 3d spin−orbit coupling, while the $^4T_{1g}(^4F)$ manifold in RXES is more sensitive to the tetragonal distortion and superexchange interactions. Differences in the nanocrystals and single crystal data were shown to be an effective smaller crystal field splitting and stronger broadening of the $^4T_{1g}(^4F)$ RXES manifold for the nanocrystals. Calculations were made to address the differences, which could best be accounted for if the parameter M was increased to 0.04 eV and the parameters $10Dq_{initial}$ and $10Dq_{intermediate}$ were decreased to 1.0 and 0.85 eV, respectively. An improved experimental resolution would not only allow for a better disentanglement of the strengths of the interactions leading to the $^4T_{1g}(^4F)$ manifold broadening, but it would also allow the observance of anti-Stokes related RXES features. Finally, it was reported that the calculations reproduced polarization-dependent measurements of CoO adequately.

In conclusion, this work presents the first RXES observation and interpretation of the crystal field, spin−orbit, and superexchange broadened ground state of single crystal and nanocrystalline cobalt(II) oxide.

ASSOCIATED CONTENT

Supporting Information

CoO nanocrystal characterization, estimation of cobalt ion surface fraction in the nanocrystals, energy calibration details of the RXES spectrometer, the material specific and excitation energy-dependent contributions to the $^4T_{1g}(^4F)$ manifold, nanocrystal CFM RXES calculations, and the CFM RXES plane simulation of cobalt(II) in CoO for the LV polarized geometry. This material is available free of charge via the Internet at http://pubs.acs.org.

AUTHOR INFORMATION

Corresponding Author

*E-mail: M.M.vanSchooneveld@uu.nl and F.M.F.deGroot@uu.nl. Tel: (31) 30 253 7400. Fax: (31) 30 251 1027.

Present Address

[§]Institut de Minéralogie et de Physique des Milieux Condensés, CNRS, Université Pierre et Marie Curie, 4 Place Jussieu, 75252 Paris Cedex 5, France

Notes

The authors declare no competing financial interest.

ACKNOWLEDGMENTS

This work was financially supported by a VICI grant (F.M.F.d.G.) of The Netherlands Organization for Scientific Research (NWO-CW). The XAS and RXES measurements were performed at the ADRESS beamline of the Swiss Light Source, using the SAXES instrument jointly built by Paul Scherrer Institut, Switzerland and Politecnico di Milano, Italy. The authors thank the Swiss spallation neutron source SINQ, Paul Scherrer Institute, Switzerland for allowing them to work in their chemistry laboratory.

REFERENCES

(1) Ramirez, A. P. *J. Phys.: Condens. Matter* **1997**, *9*, 8171.
(2) Dagotto, E. *Rev. Mod. Phys.* **1994**, *66*, 763.
(3) de Groot, F. M. F.; Kotani, A. *Core Level Spectroscopy of Solids*; CRC Press: Boca Raton, FL, 2008.
(4) Gel'mukhanov, F.; Ågren, H. *Phys. Rev. A* **1994**, *49*, 4378.
(5) Fuggle, J. C.; Alvarado, S. F. *Phys. Rev. A* **1980**, *22*, 1615.
(6) de Groot, F. M. F.; Fuggle, J. C.; Thole, B. T.; Sawatzky, G. A. *Phys. Rev. B* **1990**, *42*, 5459.
(7) Zaanen, J.; Sawatzky, G. A.; Allen, J. W. *Phys. Rev. Lett.* **1985**, *55*, 418.
(8) Wells, A. F. *Structural Inorganic Chemistry*; Clarendon Press: London, UK, 1950.
(9) Henry La Blanchetais, C. *J. Phys. Radium* **1951**, *12*, 765.
(10) Silinsky, P. S.; Seehra, M. S. *Phys. Rev. B* **1981**, *24*, 419.
(11) Rooksby, H. P.; Tombs, N. C. *Nature* **1951**, *167*, 364.
(12) van Elp, J.; Wieland, J. L.; Eskes, H.; Kuiper, P.; Sawatzky, G. A.; de Groot, F. M. F.; Turner, T. S. *Phys. Rev. B* **1991**, *44*, 6090.
(13) de Graaf, C.; de Jong, W. A.; Broer, R.; Nieuwpoort, W. C. *Chem. Phys.* **1998**, *237*, 59.
(14) Pratt, G. W., Jr.; Coelho, R. *Phys. Rev.* **1959**, *116*, 281.
(15) Newman, R.; Chrenko, R. M. *Phys. Rev.* **1959**, *115*, 1147.
(16) Kant, C.; Rudolf, T.; Schrettle, F.; Mayr, F.; Deisenhofer, J.; Lunkenheimer, P.; Eremin, M. V.; Loidl, A. *Phys. Rev. B* **2008**, *78*, 245103.
(17) de Groot, F. M. F.; Abbate, M.; van Elp, J.; Sawatzky, G. A.; Ma, Y. J.; Chen, C. T.; Sette, F. *J. Phys.: Condens. Matter* **1993**, *5*, 2277.
(18) Haverkort, M. W.; Hu, Z.; Tanaka, A.; Ghiringhelli, G.; Roth, H.; Cwik, M.; Lorenz, T.; Schüßler-Langeheine, C.; Streltsov, S. V.; Mylnikova, A. S.; Anisimov, V. I.; de Nadai, C.; Brookes, N. B.; Hsieh, H. H.; Lin, H. J.; Chen, C. T.; Mizokawa, T.; Taguchi, Y.; Tokura, Y.; Khomskii, D. I.; Tjeng, L. H. *Phys. Rev. Lett.* **2005**, *94*, 056401.
(19) Sakurai, J.; Buyers, W. J. L.; Cowley, R. A.; Dolling, G. *Phys. Rev.* **1968**, *167*, 510.
(20) Haβel, M.; Kuhlenbeck, H.; Freund, H. J.; Shi, S.; Freitag, A.; Staemmler, V.; Lütkehoff, S.; Neumann, M. *Chem. Phys. Lett.* **1995**, *240*, 205.
(21) Ghiringhelli, G.; Matsubara, M.; Dallera, C.; Fracassi, F.; Tagliaferri, A.; Brookes, N. B.; Kotani, A.; Braicovich, L. *Phys. Rev. B* **2006**, *73*, 035111.
(22) Ghiringhelli, G.; Matsubara, M.; Dallera, C.; Fracassi, F.; Tagliaferri, A.; Brookes, N. B.; Kotani, A.; Braicovich, L. *Phys. Rev. B* **2008**, *78*, 117102.
(23) Ghiringhelli, G.; Piazzalunga, A.; Dallera, C.; Schmitt, T.; Strocov, V. N.; Schlappa, J.; Patthey, L.; Wang, X.; Berger, H.; Grioni, M. *Phys. Rev. Lett.* **2009**, *102*, 027401.
(24) Ghiringhelli, G.; Piazzalunga, A.; Wang, X.; Bendounan, A.; Berger, H.; Bottegoni, F.; Christensen, N.; Dallera, C.; Grioni, M.;

Grivel, J. C.; Moretti Sala, M.; Patthey, L.; Schlappa, J.; Schmitt, T.; Strocov, V.; Braicovich, L. *Eur. Phys. J. Spec. Top.* **2009**, *169*, 199.
(25) Magnuson, M.; Butorin, S. M.; Guo, J. H.; Nordgren, J. *Phys. Rev. B* **2002**, *65*, 205106.
(26) Chiuzbăian, S. G.; Schmitt, T.; Matsubara, M.; Kotani, A.; Ghiringhelli, G.; Dallera, C.; Tagliaferri, A.; Braicovich, L.; Scagnoli, V.; Brookes, N. B.; Staub, U.; Patthey, L. *Phys. Rev. B* **2008**, *78*, 245102.
(27) Wiedwald, U.; Fauth, K.; Heßler, M.; Boyen, H. G.; Weigl, F.; Hilgendorff, M.; Giersig, M.; Schütz, G.; Ziemann, P.; Farle, M. *ChemPhysChem* **2005**, *6*, 2522.
(28) Thornton, J. M. C.; Williams, R. H. *Phys. Scr.* **1990**, *41*, 1047.
(29) Dumas, P.; Chabal, Y. J.; Jakob, P. *Surf. Sci.* **1992**, *269−270*, 867.
(30) Fuggle, J. C.; Mårtensson, N. *J. Electron Spectrosc. Relat. Phenom.* **1980**, *21*, 275.
(31) Ghiringhelli, G.; Piazzalunga, A.; Dallera, C.; Trezzi, G.; Braicovich, L.; Schmitt, T.; Strocov, V. N.; Betemps, R.; Patthey, L.; Wang, X.; Grioni, M. *Rev. Sci. Instrum.* **2006**, *77*, 113108.
(32) Strocov, V. N.; Schmitt, T.; Flechsig, U.; Schmidt, T.; Imhof, A.; Chen, Q.; Raabe, J.; Betemps, R.; Zimoch, D.; Krempasky, J.; Wang, X.; Grioni, M.; Piazzalunga, A.; Patthey, L. *J. Synchrotron Radiat.* **2010**, *17*, 631.
(33) Cowan, R. D. *J. Opt. Soc. Am.* **1968**, *58*, 808.
(34) Thole, B. T.; Van Der Laan, G.; Butler, P. H. *Chem. Phys. Lett.* **1988**, *149*, 295.
(35) Cowan, R. D. *The Theory of Atomic Structure and Spectra*; University of California Press: Berkeley, CA, 1981.
(36) Ikeno, H.; de Groot, F. M. F.; Stavitski, E.; Tanaka, I. *J. Phys.: Condens. Matter* **2009**, *21*, 104208.
(37) Stavitski, E.; de Groot, F. M. F. *Micron* **2010**, *41*, 687.
(38) Griffith, J. S. *The theory of transition metal ions*; Cambridge University Press: Cambridge, UK, 1964.
(39) Kramers, H.; Heisenberg, W. *Z. Phys.* **1925**, *31*, 681.
(40) Glatzel, P.; Bergmann, U. *Coord. Chem. Rev.* **2005**, *249*, 65.
(41) Cramer, S. P.; de Groot, F. M. F.; Ma, Y.; Chen, C. T.; Sette, F.; Kipke, C. A.; Eichhorn, D. M.; Chan, M. K.; Armstrong, W. H. *J. Am. Chem. Soc.* **1991**, *113*, 7937.
(42) Haynes, W. M.; Lide, D. R. *CRC Handbook of Chemistry and Physics*, 92nd internet ed.; CRC Press: Boca Raton, FL, 2012.
(43) Ghiringhelli, G.; Brookes, N. B.; Annese, E.; Berger, H.; Dallera, C.; Grioni, M.; Perfetti, L.; Tagliaferri, A.; Braicovich, L. *Phys. Rev. Lett.* **2004**, *92*, 117406.
(44) Tanabe, Y.; Sugano, S. *J. Phys. Soc. Jpn.* **1954**, *9*, 753.
(45) Lever, A. B. P. *Inorganic Electronic Spectroscopy*, 2nd ed.; Elsevier: Amsterdam, The Netherlands, 1984; Vol. 33.
(46) Tanabe, Y.; Sugano, S. *J. Phys. Soc. Jpn.* **1954**, *9*, 766.
(47) Ament, L. J. P.; van Veenendaal, M.; Devereaux, T. P.; Hill, J. P.; van den Brink, J. *Rev. Mod. Phys.* **2011**, *83*, 705.
(48) Butorin, S. M. *J. Electron Spectrosc. Relat. Phenom.* **2000**, *110−111*, 213.
(49) Matsubara, M.; Uozumi, T.; Kotani, A.; Parlebas, J. C. *J. Phys. Soc. Jpn.* **2005**, *74*, 2052.
(50) Flato, M. *J. Mol. Spectrosc.* **1965**, *17*, 300.
(51) Tanaka, S.; Kotani, A. *J. Phys. Soc. Jpn.* **1993**, *62*, 464.
(52) Pothuizen, J. J. M.; Cohen, O.; Sawatzky, G. A. *MRS Proc.* **1995**, *401*, 501.
(53) den Breejen, J. P.; Frey, A. M.; Yang, J.; Holmen, A.; van Schooneveld, M. M.; de Groot, F. M. F.; Stephan, O.; Bitter, J. H.; de Jong, K. P. *Top. Catal.* **2011**, *54*, 768.
(54) van Schooneveld, M. M.; Gloter, A.; Stephan, O.; Zagonel, L. F.; Koole, R.; Meijerink, A.; Mulder, W. J. M.; de Groot, F. M. F. *Nat. Nanotechnol.* **2010**, *5*, 538.
(55) Hu, Z.; Kaindl, G.; Warda, S. A.; Reinen, D.; de Groot, F. M. F.; Müller, B. G. *Chem. Phys.* **1998**, *232*, 63.
(56) We used D = 4Ds, M = 6J, and $\lambda = \zeta_{3d}/2S$ with $S = {}^3/_2$.
(57) Solomon, E. I.; Lever, A. B. P. *Inorganic electronic structure and spectroscopy−Methodology*, 2nd ed.; John Wiley & Sons, Inc.: Hoboken, NJ, 2006; Vol. *1*.
(58) Kurian, R.; van Schooneveld, M. M.; Vankó, G.; de Groot, F. M. F. Unpublished results.